Femtosecond Charge Injection Dynamics at Hybrid Perovskite Interfaces

Giulia Grancini * [a], Daniele Viola [b], Yonghui Lee [a], Michael Saliba [a], Sanghyun Paek [a], Kyung Taek Cho [a], Simonetta Orlandi [c], Marco Cavazzini [c], Fernando Fungo [d], Mohammad I. Hossain [e], Abdelhak Belaidi [e], Nouar Tabet [e], Gianluca Pozzi [c], Giulio Cerullo [b], Mohammad Khaja Nazeeruddin * [a]

Abstract: With power conversion efficiency (PCE) exceeding 22%, perovskite solar cells (PSCs) have thrilled the photovoltaic research. However, interface behavior is still not understood and a hot subject of research: different processes occur over a hierarchy of timescales, from femtoseconds to seconds, making the perovskite interface physics intriguing. Here, by femtosecond transient absorption spectroscopy with spectral coverage extended to the crucial IR region, we interrogate the ultrafast *interface- specific* processes at standard as well as newly molecularly-engineered perovskite interfaces used in state of the art PSCs. We demonstrate that ultrafast interfacial charge injection happens with a time constant of 100 fs, resulting in hot transfer from energetic charges and setting the time-scale for the first step involved in the complex charge transfer process. This also stems true for 20% efficient devices measured under real operation, where the femtosecond injection is followed by a slower picosecond component. Our findings provide compelling evidence of the femtosecond interfacial charge injection step demonstrating a robust method for a straightforward identification of the interfacial non-equilibrium processes at ultrafast timescale.

Introduction

The last few years have witnessed a breakthrough in mixed-halide PSCs, with an unexpected leap of the PCE.[1–3] These cells share a common design, where the perovskite layer is sandwiched in between the selective charge extracting layers, as sketched in Figure 1a.[2,4] Electron injection occurs into TiO_2, while different hole transporting materials (HTMs) can be used for hole injection [5]. Interfaces within the device stack thus regulate the photovoltaic behaviour and ultimately the device performances.[5] The exact mechanisms therein are still hotly debated. On the one hand, it has been demonstrated that free charges are generated within the perovskite layer itself, producing a large photovoltage without the need of a proper interface to split the charges.[5-7] On the other hand, material and interface engineering [8-9] has been a successful route to improve interfacial charge transfer and obtain highly efficient devices. A complex photophysical scenario governs the PSC device operation, due to the interplay of different concomitant processes such as exciton versus charge physics, [10-13] charge injection, recombination[11-18], accumulation[20], light- and field-induced ion movement [5, 19-21] and photo-ferroelectricity[22] with the associated changes in the material structure and optoelectronic properties[5, 23, 24]. Such processes happen on a hierarchy of different time scales, from sub-picosecond to minutes[5,25]. Understanding and controlling their dynamics is therefore essential to derive rational guidelines for development of PSC devices. Aware of such complexity, here we aim to target the initial *interface-specific* processes that follow light absorption on an ultrafast timescale directly on state of the art perovskite solar cells interfaces. The analysis focuses on standard perovskite/mesoporous TiO_2 and perovskite/HTM interfaces embodied in high efficiency devices, as well as on a novel molecularly- engineered interfaces where the HTM has been specifically designed to improve the interfacial electronic interactions and favor hole transfer. Our results demonstrate that a fraction of electrons is injected on an ultrafast, sub-picosecond timescale to the mesoporous TiO_2 as the first step of the complex light-to-current conversion mechanism. Hole transfer happens on a similar timescale, too. Notably, for the newly developed perovskite/HTM interface charge transfer happens with a time constant of τ=100 fs from highly energetic, not thermalized charges. This stems true also monitoring the interface physics in state-of-the-art PSCs during operation. Ultrafast injection manifests as well, along with a slower picosecond component limitied by charge diffusion in the bulk. Our results provide a complete analysis of the ultrafast processes, whose knowledge is fundamental to guide material and interface engineering, and of utmost importance for device optimization even beyond photovoltaics.

[a] Dr. G. Grancini, Dr. Y. Lee, Dr. M. Saliba, Dr. S. Paek, Mr. K. Cho, Prof. M.k. Nazeeruddin Group for Molecular Engineering of Functional Materials, Institute of Chemical Sciences and Engineering, Ecole Polytechnique Fédérale de Lausanne, CH-1951 Sion, Switzerland E-mail: giulia.grancini@epfl.ch
[b] Dr. D. Viola, Prof. G. Cerullo Istituto di Fotonica e Nanotecnologie del CNR, Dipartimento di Fisica, Politecnico di Milano, P.zza Leonardo da Vinci 32, 20133 Milano, Italy
[c] Dr. S. Orlandi, Dr. M. Cavazzini, Dr. G. Pozzi Istituto di Scienze e Tecnologie Molecolari del CNR, ISTM-CNR, via Golgi, 19, I-20133 Milano, Italy
[d] Dr. F. Fungo Departamento de Química, Universidad Nacional de Río Cuarto, Agencia Postal 3 (X5804BYA), 5800 Río Cuarto, Argentina.
[e] Dr. M. I. Hossain, Dr. A. Belaidi, Prof. N. Tabet, Qatar Environment and Energy Research Institute, Hamad Bin Khalifa University (HBKU), Qatar Foundation, Doha, 5825, Qatar

Results and Discussion

We fabricate PSCs using the mixed $MA_{(1-y)}FA_yPbI_xBr_{(3-x)}$ (MA=methylammonium, FA=formamidinium) perovskite as active layer sandwiched in between a mesoporous TiO_2 layer, acting as electron transporting material, and the organic HTM layer on top (see sketch in Figure1). The selection of HTMs includes the commonly used 2,2',7,7'-tetrakis(N,N-di-p-methoxyphenylamine)-9,9'-spirobifluorene (spiro-OMeTAD) as well as a newly synthetized HTM consisting of mixed spiro cores

containing a fluorene unit and a cyclopenta[2,1-b:3,4-b']dithiophene moiety that improves the interaction with the perovskite surface,[2] named FDT in the following (see their molecular structures in Fig. 1b). Additional information on the resulting perovskite film and crystal structure is reported in Fig. S1. Device J-V characteristics are shown in Figs. 1c, d, respectively along with the parameters listed in the figure caption. See Supporting Information and Methods for details on device preparation. We measure a PCE of 19.5(20)% in the device with Spiro-OMeTAD(FDT) HTM. Notably, the FDT molecule enhances the interfacial interaction with the perovskite surface through additional chemical adhesion improving the interfacial electronic coupling, while keeping the same energetics as the spiro-OMeTAD. [2] This results not only in a slightly higher efficiency, but, importantly, also in the hysteresis free behavior of the FDT-based device (see forward and backward J-V curves reported in Fig. 1c, d).

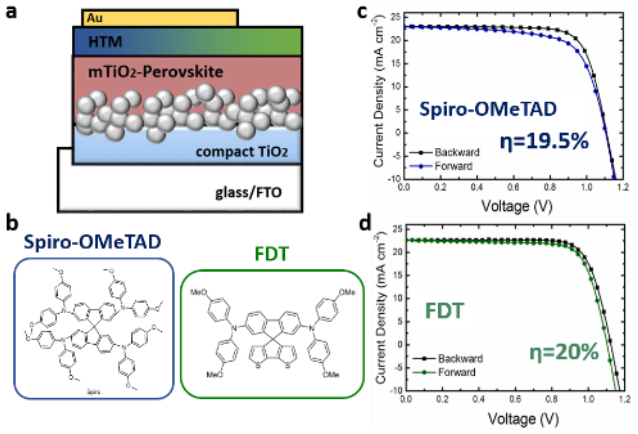

Figure 1. a. Sketch of the PSCs. **b.** Molecular structure of the HTMs used in the solar cell. **c, d.** Current/Voltage (J-V) characteristic of the PSCs with Spiro-OMeTAD and FDT, respectively, showing forward and backward scan, scan speed 10 mV/s. For SpiroOMeTAD solar cell the device parameters are: Jsc= 23.11 mA/cm^2, Voc= 1.10 V, FF= 0.687 and PCE= 17.46% in forward bias and Jsc= 23.17 mA/cm^2, Voc= 1.11 V, FF= 0.757 and PCE= 19.46% in backward bias. For FDT based solar cell: Jsc= 22.6mA/cm^2, Voc= 1.124V, FF= 0.774 and PCE= 20% in forward bias and Jsc= 22.6 mA/cm^2, Voc= 1.103 V, FF= 0.756 and PCE= 19.2% in backward bias.

To highlight the interface specific behavior, here we first monitor the single perovskite/TiO_2 and perovskite/HTM interfaces. Thin films of perovskite have been deposited on top of either TiO_2 or Al_2O_3 following the exact protocol and with the same thickness as for the high efficiency PSCs. The absorption spectra of the $MA_{(1-y)}FA_yPbI_xBr_{(3-x)}$ perovskite as well as of the perovskite /HTM heterojunctions, shown in Fig. 2, display a defined band edge at 760 nm and a similar absorbance, being all the samples around 300 nm thick (see also the cross section SEM in Fig. S1a). The absorption of the HTMs (spiro-OMeTAD and FDT) is presented in Fig. 2b, showing a peak in the blue spectral region. Fig. 2b also reports the absorption spectra of FDT and Spiro-OMeTAD chemically oxidized by Silver trifluoromethanesulfonate (AgOTf) in THF. The chemically oxidized FDT exhibits novel absorption bands at around 500 and 680 nm and an important band at 1500 nm, indicative of the formation of the oxidized species. The chemically oxidized Spiro-OMeTAD shows a very similar absorption spectrum as FDT. Notably, the absorption of the oxidized species provides the spectral signatures of the charged HTM, which will be crucial for its identification in the transient spectra, particularly for the IR-region. Aiming to understand the interface dynamics, we perform femtosecond transient absorption (TA) spectroscopy extended down to the near-IR region, a critical spectral window so far almost unexplored in perovskites. [11, 13-18, 26-31] In order to identify the main perovskite spectral signatures and the differences that might arise due to electron/hole injection, we first compare the behavior of the perovskite deposited on the injecting mesoporousTiO_2 (m-TiO_2) and on the non-injecting mesoporous Al_2O_3 (m-Al_2O_3) substrates, as shown in Fig. 3.

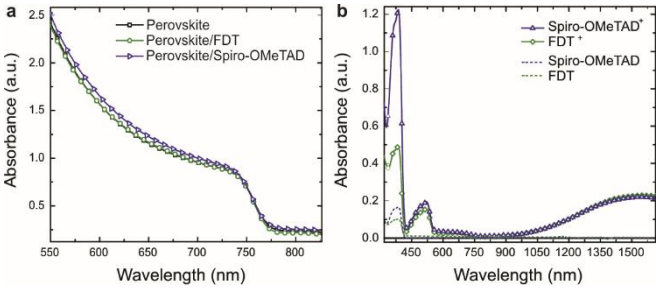

Figure 2. a. Absorption spectra of Perovskite films as well as of Perovskite/HTMs as indicated in the legend. **b.** Absorption of the Spiro-OMeTAD and FDT (dashed lines) and of the oxidized HTMs.

In both cases, exciting from the mesoporous oxide (500 nm thick), we are mainly interrogating the crystals contained in the mesoporous scaffold, thus probing the interface-specific processes, being the pump penetration depth in perovskite <100 nm. Thus the portion of electrons transferred comes from the interface, while a second contribution can also arise from the diffusing carriers form the bulk that however, considering a diffusion constant of 0.04 cm^2/s, can contribute only on a much longer timescale. [5]

We use 620 nm to excite the perovskite above the band edge with a pump fluence lower than 1μJ/cm^2 which, given the sample optical density and the film thickness (from Fig. 2a and the cross-sectional SEM image in Fig. S1) corresponds to an average carrier density of 6x10^{17} cm^{-3}. Differently from previous studies that only focused on the visible region, [26-31] the near-IR spectral window enables us to highlight the complex interface processes identifying the photoexcited states species and dynamics never explored so far in literature. Fig. 3a shows differential transmission (ΔT/T) spectra measured on the m-Al_2O_3substrate (dynamics at selected probe wavelengths are reported in Fig. 3b). In the visible range, in agreement with established literature, [11, 13-19, 26-31] [1] the spectra are dominated by a positive band peaking around 760 nm with a tail extending towards 710 nm. The band at 760 nm is assigned to photobleaching (PB) due to state filling. It rises with a time constant of τ=160 fs as indicated in Fig. 3b (red dotted line). As the PB rises the signal at 720 nm, assigned to PB

of hot carriers, decays reflecting the cooling of the hot electrons and holes. The photoinduced carriers cause the bandgap to renormalize (band gap renormalization BGR), resulting in a red-shifted absorption. This manifests in the appearance of the negative photoinduced absorption (PA) band, red-shifted with respect to the main PB peak, above 760 nm (see Figs. 3a, b) visible only within few hundreds of fs; this PA band is also a, marker of hot carriers. [26, 27] Note that hot phonon bottleneck, i.e. slow thermalization, has been observed for $CH_3NH_3PbI_3$ perovskite extending to hundreds of ps for high excitation density (around 10^{19} cm^{-3}) resulting in a non-equilibrium phonon population. [27] In the near-IR region, the $\Delta T/T$ signal displays a broad positive band extending down to 1500 nm that forms within the first picosecond (see dynamics in Fig. 3b). This positive band appears every time the perovskite is deposited on a non-injecting substrate, being either mesoporous Al_2O_3 or even glass. We assign this band to the PB or possibly stimulated emission from trap states that form at the perovskite surface or at the interface with the non-injecting substrate, and are populated within 1 ps. Note indeed that the choice of m-Al_2O_3 is dictated by the fact that in this case the perovskite crystal quality, dimension and morphology is similar to what obtained using a mesoporous injecting scaffold. This enables a fair comparison with the analysis of the TA features at the TiO_2 interface. This assignment is supported by ultraviolet photoemission spectroscopy[32] and thermal photocurrent measurements [33] that have identified the presence of a broad distribution of hole traps located ~100-400 meV below the band gap and by recent photoluminescence spectroscopy revealing shallow traps at least 20 meV within the gap. [34]

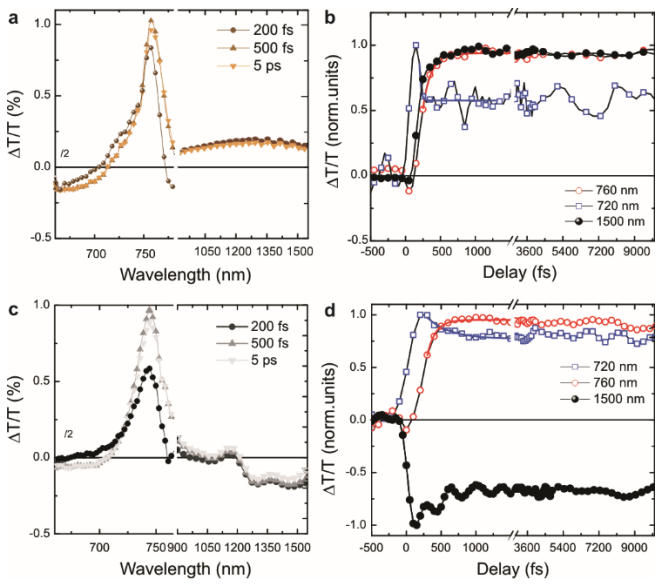

Figure 3. a, c. $\Delta T/T$ evolution from 200 fs to 5 ps upon excitation at 620 nm of the mixed perovskite deposited on non-injecting m-Al_2O_3 and on injecting m-TiO_2 respectively. **b, d.** Normalized $\Delta T/T$ dynamics at selected probe wavelengths (see legend) for $MA_{(1-y)}FA_yPbI_xBr_{(3-x)}$/ m-$Al_2O_3$ and m-TiO_2, respectively.

Our assignment also agrees with previous TA measurements reporting a broad (until 1200 nm –the longest probed wavelength) and weak PB below the optical gap that has been related to trap states having a weak oscillator strength in the ground state. [35] We consider now the $MA_{(1-y)}FA_yPbI_xBr_{(3-x)}$/m-$TiO_2$ active interface where electron transfer is expected to occur, presented in Fig. 3c. Remarkable differences, especially in the near-IR region, are observable. Considering the visible range, similarly to the case of perovskite deposited on m-Al_2O_3, the spectra are dominated by the PB due to state filling, which rises with a slightly slower time constant of ≈220 fs while the carrier population decays by 20%, (see dynamics in Fig. 3d) that can be due to interfacial Coulomb screening that decelerates the rate of phonon emission [27]. Again a combination of state filling, BGR, and spectral shift due to band gap modulation happens within the first hundreds of fs. A clear signature of electron transfer is thus rather difficult to isolate from the pure PB feature in the visible on such ultrafast time scale. The near–IR signal turns out to be much simpler to interpret: it consists of a tiny positive tail above 900 nm overlapped with a flat negative band extending at longer probe wavelengths towards 1600 nm. The positive band shows a rise completed in the first ps, similarly to what observed on the insulating m-Al_2O_3 substrate (see Fig. S2). The flat negative band, on the other hand, forms instantaneously and it is assigned to a PA of the free electrons populating the conduction band of the TiO_2 upon ultrafast electron transfer. [35] This band matches very well with the free electron absorption in TiO_2 which appears flat and usually extends out to 2300 nm. [35] It is worth mentioning that the istantaneous negative signal can overlap with the BGR tail, especially for energies just below the bandgap. On the other side, we notice that the magnitude of this band is low given the strong absorption cross section of the free electrons in TiO_2 [35], possibly indicating that we are only monitoring the fraction of photoexcited carriers at the interface, which is injected into the TiO_2 matrix at ultrafast timescales. To further confirm our spectral assignment, we performed a global analysis on the spectral evolution in the near-IR (see Fig. S2). We were able to fit the whole $\Delta T/T$ (λ, τ) spectral evolution considering only two time components (Fig. S2) associated to the positive and negative bands that can well reproduce the whole experimental data set. This measurements indicates that an ultrafast electron transfer process occurs at the perovskite/m-TiO_2 interface; however, we do not exclude a subsequent step in which charges formed in the bulk diffuse prior to reaching the interface, responsible for a slower component in the electron transfer mechanism. Remarkably, a multitude of different numbers have been reported in the early literature and associated to electron injection from perovskite to TiO_2, with time constants ranging from sub-ps to hundreds of ps[11-16, 17-18, 27-31]. However one must be careful in considering such numbers, sometimes affected by the poor quality of the perovskite film morphology, not always corresponding to a high efficiency device, or by artificiously created interfaces presented in the early literature, now surpassed. [27-31, 36-37] Additionally, specific interface functionalization using different surface treatments may also alter the electron injection rate. [38] In our case, it is important to stress that we have studied exactly the same interface used in the high-efficiency devices shown in Fig. 1. This for instance includes the

Li- passivation of the TiO_2 surface that has been demonstrated to reduce the interface trap density. [38]

Aiming now to monitor the hole transfer mechanism, we investigate the $MA_{(1-y)}FA_yPbI_xBr_{(3-x)}$/HTMs interfaces using the HTMs shown in Fig. 1. Note that the oxidized Spiro-OMeTAD and FDT show a pronounced band in the near-IR region, peaking at around 1550 nm, which can be used as spectroscopic marker to monitor the hole transfer process to the HTM, as done in the past for the study of dye-sensitized solar cell interfaces. [38, 39] The ΔT/T spectra and dynamics in the VIS and near-IR range are reported in Fig. 4 and the ΔT/T (λ, τ) maps reported in Fig. 5a, c. Excitation from the top HTM surface enables us to directly probe the HTM/perovskite specific processes.

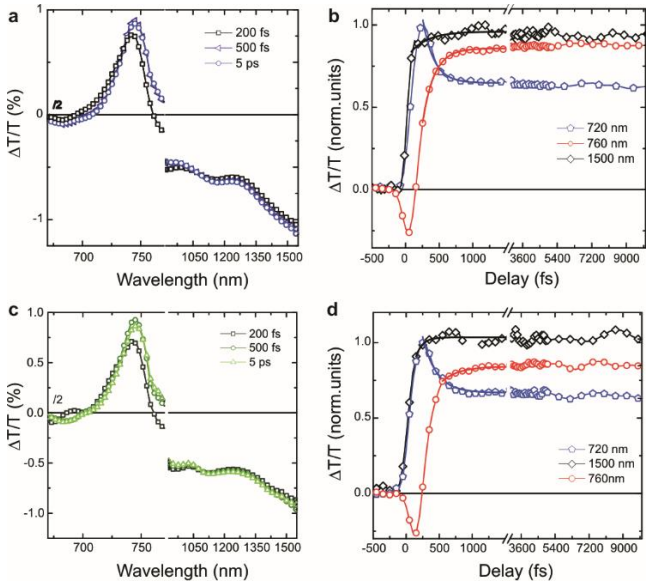

Figure 4. ΔT/T evolution from 200 fs to 1 ns upon excitation at 620 nm of the solar cell based on m-TiO_2 and **a.** spiro-OMeTAD, **c.** FDT on top. Normalized $|\Delta T/T|$ dynamics at different probe wavelengths (720 nm, 760 nm, 1550 nm) for solar cell based on m-TiO2 and **b.** spiro-OMeTAD and **d.** FDT on top.

Note that the HTMs are fully transparent at the 620 nm excitation wavelength (see Fig. 2b), thus they are not directly optically excited. For both the perovskite/HTM heterostructures, in the visible region, the PB band dominates, forming with a retrieved time constant of 180 (200) fs for Spiro-OMeTAD (FDT) which corresponds to the time for carrier thermalization. The negative sharp PA due to BGR is also evident within the first hundred of fs (see dynamics in Fig. 4b, d). On the other side, monitoring the near-IR region, an intense PA band bending towards 1550 nm is clearly observed (Fig. 4 a, c) for both the HTMs. This band well matches with the absorption of the oxidized species of the HTMs (see Fig. 2b) providing an unambiguous proof of hole injection into the HTMs. Dynamics at 1500 nm reveals that this band forms with a time constant of 100 fs for FDT (Fig. 4d) and 260 fs (Fig. 4c) for spiro-OMeTAD, demonstrating that in both cases ultrafast hole transfer occurs at the perovskite/HTM interfaces. On the other side, the absence of the PB of trap states in the near-IR TA spectra is also remarkable, indicating that the efficient interfacial interaction with the HTM and the high quality of our perovskite film limit the formation of surface trap states. To further support our spectral assignment, we performed a global analysis (see Fig. 5), enabling us to decompose the TA spectra. The global fitting considers only two temporal components to fit the entire ΔT/T (λ, τ) map (Fig. 5).

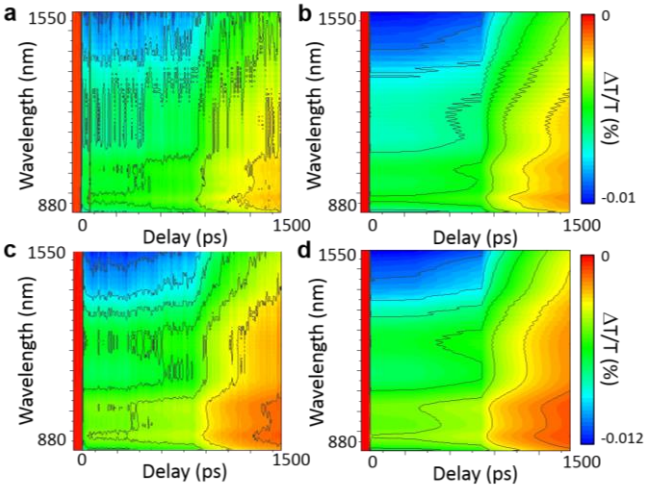

Figure 5. Comparison of the ΔT/T (λ, τ) maps (**a**) in the IR probed region and global fitting (**b**) for the Perovskite/FDT interface. Comparison of the ΔT/T (λ,τ) maps (**c**) in the IR probed region and global fitting (**d**) for the Perovskite/Spiro-OMeTAD interface. Excitation at 620 nm with a fluence of $6x10^{17}$ photons/cm^3.

The results highlight the overlap of two PA bands: one which is nearly frequency independent, similar to the one observed in the sample of $MA_{(1-y)}FA_yPbI_xBr_{(3-x)}$/m-$TiO_2$ related to the absorption of free electrons in the TiO_2, and one peaking around 1550 nm, assigned to the charged HTM, strongly confirming our interpretation. Spectral cuts of the fitted ΔT/T (λ, τ) maps are reported in Fig. S3 and Table S1. A closer inspection on the dynamics presented in Fig. 4b, c reveals that for the case of the perovskite/FDT interface the PA band rises with τ=100 fs, when photoinduced carriers still possess excess energy and are not completely thermalized. The improved interactions at the FDT/perovskite interface can thus result into a hot hole injection, suggesting that a fraction of charges can be transferred prior to thermalization. Hot carrier migration has been recently revealed [26, 27] for above gap excitation where quasi-ballistic transport correlated with the excess kinetic energy has been demonstrated. Our results on the interface processes make a step beyond suggesting that hot carriers can be harvested before they thermalize, a potential way to break the Shockley-Queisser limit and boost the device efficiency.

To generalize our finding we also measured the $MA_{(1-y)}FA_yPbI_xBr_{(3-x)}$ perovskites interfaces with standard polytriarylamine (PTAA), providing state of the art 20% efficient devices as well as a newly synthetized HTM based or a pyridine-modified fluorene core, named PEH-11 (see Fig. S4 for chemical

structures and Table S2 for device output parameters), which despite similar structure and energetics to Spiro-OMeTAD (see Table S2), does not form an efficient interface, resulting in poor device performances (around 1% efficiency, see Fig. S4 and Table S3). TA spectra for these interfaces in the near-IR are shown in Fig. S5 and S6. For the $MA_{(1-y)}FA_yPbI_xBr_{(3-x)}$ /PTAA interface an ultrafast hot hole injection happens with a time constant of 120 fs (see Fig. S5). For the PEH-11, on the other side, at very initial time scale a broad positive band appears in the near IR (previously assigned to charge trapping) that turns into a flat negative band in the first hundreds of fs (previously assigned to PA of free electrons in TiO_2), see Fig. S6b. Strikingly, the strong absorption band of the oxidized species in PEH-11, which peaks at 900 nm as shown in Fig. S6c, is not observed. This indicates that at the interface of the pyridine based HTM PEH-11 the hole transfer is hampered, despite the proper interfacial energy level alignment. Although many other components can limit the device efficiency, the absence of ultrafast hole injection is a fingerprint of a non-optimal interface, not desirable for a highly efficient device.
We performed a similar analysis also on $FAPbBr_3$ perovskite, of particular interest for the high Voc solar cells [40] as well as for light emitting optoelectronic applications. [41] We probed the ultrafast charge injection at $FAPbBr_3$/HTM interfaces considering both spiro-OMeTAD and FDT. Absorption of $FAPbBr_3$ is reported in Fig. S7. TA data are presented and discussed in Fig S8. Even in this case we observe a clear PA band in the near-IR region bending towards 1500 nm that forms within few hundreds of fs (see dynamics in Fig. S8c). This observation further confirms our analysis and enables us to generalize the main mechanism governing the interface physics at ultrafast times.
It is worth mentioning that PSCs operation is influenced by complex phenomena such as light- and field–induced ion movement and polarization effects [20-23], as well as photo-doping and photon recycling. [42, 43] These processes happen on much longer time scales, from seconds to minutes, with respect to the ultrafast processes revealed in this paper. However, to assess their possible influence on the identified interfacial charge transfer dynamics, we have measured the $\Delta T/T$ signal for the highly efficient $MA_{(1-y)}FA_yPbI_xBr_{(3-x)}$/PTAA PSC device upon applying a continuous white light illumination for one minute and then upon switching it off, without changing the position on the sample. Note that we excite from the TiO_2 layer and we record the probe signal reflected from the gold electrode, so that the $|\Delta R/R|$ signal can be interpreted, in first approximation, as a double-pass $|\Delta T/T|$ signal. We observed that the PA signal does not change neither in intensity nor in time evolution (see the dynamics in Fig. S9). This indicates that light-induced phenomena, such as "photo-doping" or "trap filling" [42, 43] do not interfere with the sub-picosecond processes here observed.
We have also monitored the charge injection dynamics in the high efficiency Spiro-OMeTAD based PSC device under different operating conditions, at short circuit (V=0) and at 1 V, close to the open circuit voltage. Spectra and dynamics are shown in Fig. S10 and S11, respectively. At 1V the dynamics show a fast quenching component with τ=200 fs (similarly to the case of not-connected device). At short circuit, the dynamics still show the fast quenching along with a second component with τ=4 ps. This suggests that, as a result of interfacial energy band bending, a new charge injection channel is activated. [35] The result further confirms that ultrafast charge injection happens at the active interface embodied in the device under operation, accompanied by a slower channel activated at short circuit conditions. This strengthens the relevance of our findings, demonstrating that ultrafast interfacial charge transfer processes also occur within state-of-the-art PSC devices.

Conclusions

In this work we have studied the ultrafast electron/hole transfer processes occurring at perovskite/TiO_2 and at different perovskite/HTM interfaces. Using state-of-the-art and novel materials and interfaces and exploiting for the first time the sensitive near-IR spectral window, we provide unambiguous evidence that interfacial electron/hole injection occur on the sub-picosecond timescale. While many other processes happening on a hierarchy of timescales play a role in driving the PSCs operation, and will be subject of future investigations, our results demonstrate that ultrafast interfacial charge injection is the primary step in efficient devices. Interestingly, at optimized interfaces, hot carriers with excess energy are transferred, competing with charge thermalization. In addition, we demonstrate that, by tuning the chemistry of the interface through molecular engineering of the HTM, the interfacial dynamics are dramatically affected leading, in some cases, to greatly reduced device efficiency. These findings reveal the complexity of chemistry and materials science in the development of novel suitable HTM materials and in interface engineering, but provide guidelines for material engineering as well as a universal method for a straight-forward identification of the best working active interfaces behind highly efficient perovskite devices.
In addition, we provide a new and robust protocol for the study of the interface physics, of utmost importance for the engineering of devices composed by perovskite interfaces even beyond photovoltaics whose optimization relies on the understanding and control of the interface physics.

Experimental Section

Solar Cell Fabrication and testing. Substrate preparation: Nippon Sheet Glass 10 Ω/sq was cleaned by sonication in 2% Hellmanex water solution for 30 minutes. After rinsing with deionised water and ethanol, the substrates were further cleaned with UV ozone treatment for 15 min. Then, 30 nm TiO_2 compact layer was deposited on Fluorine doped Tin Oxide (FTO) via spray pyrolysis at 450°C from a precursor solution of titanium diisopropoxide bis(acetylacetonate) in anhydrous ethanol. After the spraying, the substrates were left at 450°C for 45 min and left to cool down to room temperature. Then, a mesoporous TiO_2 layer was deposited by spin coating for 20 s at 4000 rpm with a ramp of 2000 rpm s^{-1}, using 30 nm particle paste (Dyesol 30 NR-D) diluted in ethanol to achieve a 150-200 nm thick layer. After the spin coating, the substrates were immediately dried at 100°C for 10 min and then sintered again at 450°C for 30 min under dry air flow. Li-doping of mesoporous TiO_2 (according to Ref. [2])is accomplished by spin coating a 0.1 M solution of bis(trifluoromethylsulfonyl)imide lithium salt (Li-TFSI) in acetonitrile at

3000 rpm for 30 s followed by another sintering step at 450°C for 30 minutes. After cooling down to 150°C the substrates were immediately transferred in a nitrogen atmosphere glove box for depositing the perovskite films.

$MA_{(1-y)}FA_yPbI_xBr_{(3-x)}$ Perovskite precursor solution and film preparation: the "mixed perovskite" $MA_{(1-y)}FA_yPbI_xBr_{(3-x)}$ precursor solution contained FAI (1 M), PbI_2 (1.1 M), MABr (0.2 M) and $PbBr_2$ (0.2 M) dissolved in anhydrous DMF:DMSO 4:1 (v:v). The respective perovskite solution was spin coated in a two steps program at 1000 and 6000 rpm for 10 and 30 s respectively. During the second step, 100 µL of chlorobenzene was poured on the spinning substrate 15 s prior to the end of the program. The substrates were then annealed at 100°C for 1 h in a nitrogen filled glove box. Hole transporting layer and top electrode: after the perovskite annealing, the substrates were cooled down for few minutes and a spirobifluorene linked methoxy triphenylamines (spiro-OMeTAD, Merck) solution (70 mM in chlorobenzene) was spin coated at 4000 rpm for 20 s. Spiro-OMeTAD was doped with bis(trifluoromethylsulfonyl)imide lithium salt (Li-TFSI, Sigma-Aldrich), tris(2-(1H-pyrazol-1-yl)-4-tert-butylpyridine)- cobalt(III) tris(bis(trifluoromethylsulfonyl)imide) (FK209, Dynamo) and 4-tert-Butylpyridine (TBP, Sigma-Aldrich). The molar ratio of additives for spiro-OMeTAD was: 0.5, 0.03 and 3.3 for Li-TFSI, FK209 and TBP respectively. The FDT solutions were prepared with molarities ranging from 50-150mM (in chlorobenzene or toluene). The optimized molar ratio of additives for FDT was: 0.5, 0.03 and 3.3 for Li-TFSI, FK209 and TBP respectively. FDT was prepared according to a procedure previously reported by us in Ref [1]. The FDT solution was spin coated at 4000 rpm for 20 s. The PTAA solution was prepared by dissolving 10 mg of PTAA (Emindex) with additives in 1 mL of toluene. As additives, 7.5 µL of Li-bis(trifluoromethanesulphonyl) imide from the stock solution (170 mg in 1 mL of acetonitrile) and 4 µL of 4-tert-butylpyridine (TBP) were added. The HTM layer was formed by spin-coating the solution at 3,000 rpm for 20 sec. Finally, 70-80 nm of gold top electrode was thermally evaporated under high vacuum. Details on the PEH-11 molecule can be found in the SI.

PV device testing. The solar cells were measured using a 450 W xenon light source (Oriel), or a commercially available solar simulator system (VERASOL, LSS-7120/LSH-7520, Oriel). The spectral mismatch between AM1.5G and the simulated illumination was reduced by the use of a Schott K113 Tempax filter (Präzisions Glas & Optik GmbH). The light intensity was calibrated with a Si photodiode equipped with an IR-cut off filter (KG3, Schott), and it was recorded during each measurement. Current-voltage characteristics of the cells were obtained by applying an external voltage bias while measuring the current response with a digital SourceMeter (Keithley 2400 or 2602B). The voltage scan rate was 10 or 25 mV s^{-1} and no device preconditioning, such as light soaking or forward voltage bias applied for long time, was applied before starting the measurement. The starting voltage was determined as the potential at which the cells furnishes 1 mA in forward bias, no equilibration time was used. The cells were masked with a black metal mask (0.16 cm^2) to fix the active area and reduce the influence of the scattered light.

Femtosecond Transient Absorption Spectroscopy. Our femtosecond TA spectrometer starts with an amplified Ti:sapphire laser, generating 4-mJ, 100 fs pulses at 800 nm wavelength and 1-kHz repetition rate. A 300-µJ fraction of the pulse energy is used for the experiments, and is split into two beams. The first beam feeds an optical parametric amplifier, generating tunable pump pulses in the visible with ≈70-fs duration; the second beam is focused in a transparent crystal, generating a broadband white-light continuum (WLC) spanning the visible and near-IR ranges and used as a probe. A 3-mm-thick sapphire plate is used to generate the WLC in the visible, while a 5-mm-thick YAG plate is used for the WLC in the near-IR. Pump and probe pulses are non-collinearly focused on the sample and the transmitted probe, spatially selected by an iris, is sent to a spectrometer (silicon for the visible range and InGaAs for the near-IR range) capable of single-shot detection at the full 1-kHz repetition rate of the laser. The differential transmission ($\Delta T/T$) spectrum is obtained by recording the probe spectrum with and without the pump pulse. The pump beam energy density used in the experiment is kept deliberately low (pump fluence less than 1 µJ/cm^2, which results in excitation densities in the order of $6x10^{17}$ cm^{-3}). All the measurements were taken with the samples encapsulated to prevent any effect from oxygen or sample degradation.

Global analysis fitting. The measured two-dimensional $\Delta T/T$ map was analyzed with a global analysis approach, based on the method presented in Refs. 44 and 45. We used a simple parallel model with 2 components to disentangle the different spectral features that can be recognized from the raw data. The analysis took in account the instrumental response function of the experiment convoluting the dynamics with a Gaussian pulse of ≈ 150 fs duration (FWHM).

Acknowledgements

G.G. has been supported by the co-funded Marie Skłodowska Curie fellowship, H2020 Grant agreement no. 665667, fund number 588072. KC acknowledge SNSF NRP 70 project; number: 407040_154056. This project has received funding from the European Union's Horizon 2020 research and innovation programme under grant agreement no 654148 Laserlab-Europe. G.C. acknowledges support by the European Research Council Advanced Grant STRATUS (ERC-2011-AdG No. 291198).

Keywords: perovskite solar cells, photovoltaics, ultrafast spectroscopy, charge injection, interface physics

References

[1] *http://www.nrel.gov/ncpv/images/efficiency_chart.jpg*.
[2] Saliba, M.; Orlandi, S.; Matsui, T.; Aghazada, S.; Cavazzini, M.; Correa-Baena, J.-P.; Gao, P.; Scopelliti, R.; Mosconi, E.; Dahmen, K.-H.; De Angelis, F.; Abate, A.; Hagfeldt, A.; Pozzi, G.; Graetzel, M.; Nazeeruddin, M. K. *Nat. Energy* 2016, **1**, 15017.
[3] Saliba, M.; Matsui, T.; Domanski, K.; Seo, J.-Y.; Ummadisingu, A.; Zakeeruddin, S. M.; Correa-Baena, J.-P.; Tress, W. R.; Abate, A.; Hagfeldt, A.; Grätzel, M. *Science* 2016, **354** (6309), 206–209.
[4] Roldán-Carmona, C.; Gratia, P.; Zimmermann, I.; Grancini, G.; Gao, P.; Graetzel, M.; Nazeeruddin, M. K. *Energy Environ. Sci.* 2015, **8** (12), 3550–3556.
[5] Stranks, S. D.; Snaith, H. J. *Nat. Nanotechnol.* 2015, **10** (5), 391–402.
[6] L. Etgar, P. Gao, Z. Xue, Q. Peng, A. K. Chandiran, B. Liu, Md. K. Nazeeruddin, M. Grätzel, *J. Am. Chem. Soc*. 2012, **134**, 17396–17399.
[7] J. H. Heo, S. H. Im, J. H. Noh, T. N. Mandal, C.-S. Lim, J. A. Chang, Y. H. Lee, H. J. Kim, A. Sarkar, Md. K. Nazeeruddin et al. *Nature Photon*., 2013, **7**, 486–491.
[8] K. T. Butler, Y. Kumagai, F. Oba, A. J. Walsh *J. Mater. Chem. C* 2016, **4**, 1149-1158.
[9] Xing, G.; Wu B., Chen, S.; Chua, J.; Yantara, N.; Mhaisalkar, S.; Mathews, N.; Sum. T. C. *Small* 2015, **11**, 3606–3613.
[10] G. Grancini, D. Viola, M. Gandini, D. Altamura, E. A. A. Pogna, V. D'Innocenzo, I. Bargigia, C. Giannini, G. Cerullo, and A. Petrozza *ACS Energy Lett.* 2017, **2** (1), 265–269.
[11] Marchioro, A.; Teuscher, J.; Friedrich, D.; Kunst, M.; van de Krol, R.; Moehl, T.; Grätzel, M.; Moser, J.-E. *Nat. Photonics* 2014, **8** (3), 250–255.

[12] Grancini, G.; Srimath Kandada, A. R.; Frost, J. M.; Barker, A. J.; De Bastiani, M.; Gandini, M.; Marras, S.; Lanzani, G.; Walsh, A.; Petrozza, A. *Nat. Photonics* 2015, **9** (10), 695–701.

[13] Price, M. B.; Butkus, J.; Jellicoe, T. C.; Sadhanala, A.; Briane, A.; Halpert, J. E.; Broch, K.; Hodgkiss, J. M.; Friend, R. H.; Deschler, F. *Nat. Commun.* 2015, **6**, 8420.

[14] Brauer, J. C.; Lee, Y. H.; Nazeeruddin, M. K.; Banerji, N. *J. Phys. Chem. Lett.* 2015, **6** (18), 3675–3681.

[15] Wu, X.; Trinh, M. T.; Niesner, D.; Zhu, H.; Norman, Z.; Owen, J. S.; Yaffe, O.; Kudisch, B. J.; Zhu, X.-Y. *J. Am. Chem. Soc.* 2015, **137** (5), 2089–2096.

[16] Douhal, A.; Piatkowski, P.; Cohen, B.; Ramos, J. F.; Nunzio, M. R. D.; Nazeeruddin; K, M.; Ahmad, M. G. and S. *Phys Chem Chem Phys* 2016, **18**, 5219-5231.

[17] Sum, T. C.; Mathews, N. *Energy Environ. Sci.* 2014, **7** (8), 2518–2534.

[18] Ponseca, C. S.; Hutter, E. M.; Piatkowski, P.; Cohen, B.; Pascher, T.; Douhal, A.; Yartsev, A.; Sundström, V.; Savenije, T. J. *J. Am. Chem. Soc.* 2015, **137** (51), 16043–16048.

[19] deQuilettes, D. W.; Zhang, W.; Burlakov, V. M.; Graham, D. J.; Leijtens, T.; Osherov, A.; Bulović, V.; Snaith, H. J.; Ginger, D. S.; Stranks, S. D. *Nat. Commun.* 2016, **7**, 11683.

[20] Zhao, Y.; Liang, C.; Zhang, H.; Li, D.; Tian, D.; Li, G.; Jing, X.; Zhang, W.; Xiao, W.; Liu, Q.; Zhang, F.; He, Z. *Energy Environ. Sci.* 2015, **8** (4), 1256–1260.

[21] Xiao, Z.; Yuan, Y.; Shao, Y.; Wang, Q.; Dong, Q.; Bi, C.; Sharma, P.; Gruverman, A.; Huang, J. *Nat. Mater.* 2015, **14** (2), 193–198.

[22] Liao, W.-Q.; Zhang, Y.; Hu, C.-L.; Mao, J.-G.; Ye, H.-Y.; Li, P.-F.; Huang, S. D.; Xiong, R.-G. *Nat. Commun.* 2015, **6**, 7338.

[23] Saparov, B.; Mitzi, D. B. *Chem. Rev.* 2016, *116* (7), 4558–4596.

[24] Yoon, S. J.; Draguta, S.; Manser, J. S.; Sharia, O.; Schneider, W. F.; Kuno, M.; Kamat, P. V. *ACS Energy Lett.* 2016, **1**, 290−296

[25] Park, N.-G.; Grätzel, M.; Miyasaka, T.; Zhu, K.; Emery, K. *Nat. Energy* 2016, **1,** 16152.

[26] Z. Guo, Y. Wan, M. Yang, J. Snaider, K. Zhu, L. Huang *Science* 2017 **356** (6333), 59-62.

[27] Y. Yang, D. P. Ostrowski, R. M. France, K. Zhu, J. van de Lagemaat, J. M. Luther & M. C. Beard *Nat. Photonics* 2016, **10**, 53–59 (2016)

[28] Q. Shen, Y. Ogomi, J. Chang, S. Tsukamoto, K. Kukihara, T. Oshima *Phys. Chem. Chem. Phys.* (2014) **16**, 19984-19992

[29] J. C. Brauer, Y. H. Lee, M.d Khaja Nazeeruddin, N. Banerji *J. Phys. Chem. Lett.* (2015) **6**, 3675-3681

[30] D. Zhong, B. Cai, X. Wang, Z. Yang, Y. Xing, S. Miao, W.-H. Zhang, C. Li *Nano Energy* (2015) **11**, 409-418

[31] T. J. Jacobsson, J.-P. Correa-Baena, E. H. Anaraki, B. Philippe, S.D. Stranks, M. E. F. Bouduban, W. Tress, K.Schenk, J. Teuscher, J.-E. Moser, H. Rensmo and A.Hagfeldtl *J. Am. Chem. Soc.,* 2016, **138** (32), 10331–10343

[32] S. Nah, B. Spokoyny, C. Stoumpos, C. M. M. Soe, M. Kanatzidis & E. Harel. *Nature Photonics* 2017, **11**, 285–288

[33] Baumann, A.; Väth, S.; Rieder, P.; Heiber, M. C.; Tvingstedt, K.; Dyakonov, V. *J. Phys. Chem. Lett.* 2015, **6** (12), 2350–2354.

[34] Srimath Kandada, A. R.; Neutzner, S.; D'Innocenzo, V.; Tassone, F.; Gandini, M.; Akkerman, Q. A.; Prato, M.; Manna, L.; Petrozza, A.; Lanzani, G. *J. Am. Chem. Soc.* 2016, **138** (41), 13604–13611.

[35] Tamaki, Y.; Furube, A.; Murai, M.; Hara, K.; Katoh, R.; Tachiya, M. *Phys. Chem. Chem. Phys.* 2007, **9** (12), 1453–1460.

[36] Shen, Q.; Ogomi, Y.; Chang, J.; Tsukamoto, S.; Kukihara, K.; Oshima, T.; Osada, N.; Yoshino, K.; Katayama, K.; Toyoda, T.; Hayase, S. *Phys. Chem. Chem. Phys.* 2014, **16** (37), 19984–19992.

[37] Xing, G.; Wu, B.; Chen, S.; Chua, J.; Yantara, N.; Mhaisalkar, S.; Mathews, N.; Sum, T. C. *Small* 2015, **11** (29), 3606–3613.

[38] Giordano, F.; Abate, A.; Baena, J. P. C.; Saliba, M.; Matsui, T.; Im, S. H.; Zakeeruddin, S. M.; Nazeeruddin, M. K.; Hagfeldt, A.; Graetzel, M. *Nat. Commun.* 2016, **7**, 10379.

[39] Bi, D.; Yang, L.; Boschloo, G.; Hagfeldt, A.; Johansson, E. M. J. *J. Phys. Chem. Lett.* 2013, **4** (9), 1532–1536.

[40] N. Arora, S. Orlandi, M. I. Dar, S. Aghazada, G. Jacopin, M. Cavazzini, E. Mosconi, P. Gratia, F. De Angelis, G. Pozzi, M. Graetzel, M.K. Nazeeruddin *ACS Energy Lett.*, 2016, **1** (1), 107–112.

[41] Z. K. Tan, R. S. Moghaddam, M. L. Lai, P. Docampo, R. Higler, F. Deschler, M. Price, A. Sadhanala, L. M. Pazos, D. Credgington, F. Hanusch, T. Bein, H. J. Snaith, R. H. Friend *Nature Nanotechnology* 2014, **9**, 687–692.

[42] T. Hoke, E.; J. Slotcavage, D.; R. Dohner, E.; R. Bowring, A.; I. Karunadasa, H.; D. McGehee, M. *Chem. Sci.* 2015, **6** (1), 613–617.

[43] Pazos-Outón, L. M.; Szumilo, M.; Lamboll, R.; Richter, J. M.; Crespo-Quesada, M.; Abdi-Jalebi, M.; Beeson, H. J.; Vrućinić, M.; Alsari, M.; Snaith, H. J.; Ehrler, B.; Friend, R. H.; Deschler, F. *Science* 2016, **351** (6280), 1430–1433.

[44] W. Ken-Tsung; C. Ruei-Tan; F. Fu-Chuan; W. Chung-chih, L. Yu-Ting *Organic Letters* 2005, **7,** 1979-1982.

[45] I. H. M. Van Stokkum; D. S. Larsen, R. van Grondelle *Biochim. Biophys. Acta* 2004, **1657**, 82−104.